GEOFLUIDS
Geofluids (2015) doi: 10.1111/gfl.12146

Post-CO_2 injection alteration of the pore network and intrinsic permeability tensor for a Permo-Triassic sandstone

M. R. HALL[1,2], S. P. RIGBY[3], P. DIM[3], K. BATEMAN[2], S. J. MACKINTOSH[4,*] AND C. A. ROCHELLE[2]

[1]*Nottingham Centre for Geomechanics, Division of Materials, Mechanics and Structures, Faculty of Engineering, University of Nottingham, Nottingham, UK;* [2]*British Geological Survey, Environmental Science Centre, Nottingham, UK;* [3]*Division of Manufacturing and Process Technologies, Faculty of Engineering, University of Nottingham, Nottingham, UK;* [4]*Department of Energy and Climate Change, UK Government, London, UK*

ABSTRACT

The aim of this study was to determine the process–structure–property relationships between the pre- and post-CO_2 injection pore network geometry and the intrinsic permeability tensor for samples of core from low-permeability Lower Triassic Sherwood Sandstone, UK. Samples were characterised using SEM-EDS, XRD, MIP, XRCT and a triaxial permeability cell both before and after a three-month continuous-flow experiment using acidic CO_2-rich saline fluid. The change in flow properties was compared to those predicted by pore-scale numerical modelling using an implicit finite volume solution to the Navier–Stokes equations. Mass loss and increased secondary porosity appeared to occur primarily due to dissolution of intergranular cements and K-feldspar grains, with some associated loss of clay, carbonate and mudstone clasts. This resulted in a bulk porosity increase from 18 to 25% and caused a reduction in mean diameter of mineral grains with an increase in apparent pore wall roughness, where the fractal dimension, D_f, increased from 1.68 to 1.84. All significant dissolution mass loss occurred in pores above *c.* 100 μm mean diameter. Relative dilation of post-treatment pore area appeared to increase in relation to initial pore area, suggesting that the rate of dissolution mass loss had a positive relationship with fluid flow velocity; *that is,* critical flow pathways are preferentially widened. Variation in packing density within sedimentary planes (occurring at cm-scale along the -*z* plane) caused the intrinsic permeability tensor to vary by more than a factor of ten. The bulk permeability tensor is anisotropic having almost equal value in -*z* and -*y* planes but with a 68% higher value in the -*x* plane (parallel to sedimentary bedding planes) for the pretreated sample, reducing to only 30% higher for the post-treated sample. The intrinsic permeability of the post-treatment sample increased by one order of magnitude and showed very close agreement between the modelled and experimental results.

Key words: carbon capture and storage, carbon dioxide, CO_2, fluid transport modelling, pore network modelling, sandstone, underground storage, X-ray CT

Received 19 September 2014; accepted 21 May 2015

Corresponding author: Matthew R. Hall, Nottingham Centre for Geomechanics, Division of Materials, Mechanics and Structures, Faculty of Engineering, University of Nottingham, University Park, Nottingham NG7 2RD, UK. Email: matthew.hall@nottingham.ac.uk. Tel: +44 115 846 7873. Fax: +44 115 951 3159,

Geofluids (2015)

INTRODUCTION

Delivering secure, affordable electricity, whilst meeting ambitious greenhouse gas reduction targets, is a global priority and carbon capture and storage (CCS) has the potential to be one of the most cost-effective technologies for decarbonisation of the power and industrial sectors (Metz *et al.* 2005). CCS technology captures carbon dioxide (CO_2) emissions created by the combustion of fossil fuels in power stations and in a variety of industrial processes and transports it for safe, long-term storage (>1000 years) in suitable deep geological formations such as depleted oil and gas reservoirs, deep saline aquifer formations in sedimentary basins, and within and around unmineable coal seams. CCS is still unproven at commercial

*Affiliation when work was conducted: Faculty of Engineering, University of Nottingham, University Park, Nottingham NG7 2RD, UK

scale although one project in Canada has recently become operational. Boundary Dam is a postcombustion coal plant, which will store CO_2 separated from the coal-fired power plant by reinjection into a saline formation (approximately 1Mt per year). In the UK, the government is providing financial support to two major CCS projects through the government-supported CCS Commercialisation competition. Both projects are planning to store the CO_2 offshore in the North Sea: the Peterhead project in a depleted gas reservoir and the White Rose project in a saline aquifer. Understanding the long-term behaviour of CO_2 in a reservoir is a key goal for both projects to minimise any future risk of unexpected CO_2 migration. Reservoir models will play a significant role in predicting the long-term movement of CO_2, both during and after injection and in verifying the long-term containment of the injected CO_2; therefore, it is imperative that the models include as much data as possible to make them accurate. This is more challenging for storage in a saline aquifer than the depleted gas reservoir because the saline reservoirs do not have exploration or production data to input into the model.

Both CCS Commercialisation projects are planning to store CO_2 in Permo-Triassic sandstone reservoirs, which are important oil and gas reservoirs and are the UK's primary resource for gas storage and for prospective geological storage of CO_2 due to their relatively high porosity, high permeability and good pH-buffering ability (Brook *et al.* 2003; Rochelle *et al.* 2004; Armitage *et al.*, 2011). Geological storage of CO_2 occurs through a combination of physical and chemical trapping mechanisms that are effective over different time frames and scales (Gunter *et al.* 1993; Holloway 1996). CO_2 can be trapped as a dissolved phase (solubility trapping), and once in solution, it can become adsorbed onto mineral surfaces (adsorption trapping) or react with the rock matrix to produce secondary carbonate phases (mineral trapping) (Bachu *et al.* 2007). The latter can effectively immobilise the CO_2 for 'geological timescales'. The extent of mineral trapping in the reservoir depends largely on the *in situ* mineralogy, pressure, temperature, pH, rate of injection of the CO_2 (Matter & Keleman 2009) and the extent of CO_2–water mixing. Spatial distribution and temporal evolution of the CO_2 injection along with the associated mineral dissolution and precipitation from the rock–fluid interactions could have a significant impact on injection performance and storage capacity and security (Leith *et al.* 1996; Xiao *et al.* 2009). The chemistry of the formation waters is the result of different hydrogeochemical processes such as mixing, dissolution and precipitation of minerals, bacterial activity and interactions with organics (Gaus *et al.* 2008). After injection, the dissolution of CO_2 acidifies formation water through the linked equilibria given in Eq. 1:

$$CO_2(aq) + H_2O = H_2CO_3 = HCO_3^- + H^+ = CO_3^{2-} + 2H^+ \quad (1)$$

It should be noted, however, that significant amounts of carbonate ions (CO_3^{2-}) will only exist where pore waters are sufficiently alkaline. Given that the storage environment will contain significant amounts of CO_2 that will cause acidification of pore waters, then it is very unlikely that carbonate ions will be formed. It is also unlikely that much true carbonic acid will exist. Inorganic carbon will therefore largely exist as $CO_{2(aq)}$ and bicarbonate ions (HCO_3^-) in a slightly acidified pore water. Migration of a CO_2-rich fluid can lead to geochemical reactions in reservoir rock (Gunter *et al.* 1993; Czernichowski-Lauriol *et al.* 1996), which for sandstones would initially include acid dissolution of the carbonate cements and reactive silicate minerals such as K-feldspars and latterly (if sufficient quantities exist) precipitation and subsequent carbonation of metal cations (*e.g.* Ca^{2+}, Mg^{2+}) as secondary carbonate minerals. Interparticle sandstone pores are disordered and irregular, and they do not follow the Euclidean description (*i.e.* using integer dimensions that do not vary with respect to the unit of measurement used) due to the scale-dependent measures of length, area and volume (Katz & Thompson 1985; Chun *et al.* 2008). These objects are called fractals, and the dimensions of such objects are nonintegral and defined as fractal dimensions (Mandelbrot 1982). The measure of a fractal object, $M(L)$, is related to the length scale, L, through a scaling law in the form of $M(L) \sim L^{Df}$, where M can be the length of a line or the area of a surface or the volume of a cube or the mass of an object, and D_f is the fractal dimension of an object (Yu & Cheng 2002). This implies the property of self-similarity, which means that the value of D_f is a constant over a range of length scales, L. Good agreement exists between D_f determined by the standard box count method and Eq. 2, for bidispersed packed granular media (Yu & Cheng 2002), if the relative proportions of bulk porosity and microporosity are known.

$$D_f = 2 + \frac{\ln \phi}{\ln\left(d^+\sqrt{(1-n_i)/(2(1-n))}\right)} \quad (2)$$

Note that n_i (microporosity) is defined here as ≤10 μm diameter. The term $d^+ = 2R_c/d_0$, where R_c is the characteristic radius of the particle cluster and d_0 the minimum particle diameter. From a given D_f, good experimental agreement has been observed for the predicted fractal permeability model (Yu & Cheng 2002; Yu *et al.* 2005) summarised in Eq. 3, where $d^+ = 2R/d_0$, including the special case of monodispersed packed granular media where $n_i = 0$.

$$k = \frac{\pi}{128}\frac{L_0^{1-D_T}}{A}\frac{D_f}{3+D_T-D_f}\overline{\lambda}_{\max}^{3+D_T} \quad (3)$$

However, for complex multiscale pore networks such as natural sandstones, the approach is not currently proven and cannot account for the associated heterogeneities such as large pore throat/cavity ratios, *that is* saccate or 'ink bottle' pores. Some previous studies have applied mesh-free techniques, including the Lattice Boltzmann and Monte Carlo methods (Quispe *et al.* 2005; Vidal *et al.* 2009), to conduct pore-scale fluid flow simulations. A method previously proposed by Radlinski *et al.* (2004), modified by Padhy *et al.* (2007) and then adopted by Amirtharaj *et al.* (2011) enables quantitative analysis of data for a series of sandstones using a method that combines information from thin section micrographs of the pore space with mercury intrusion porosimetry (MIP) in a statistical framework. They used this approach to estimate pore throat/cavity ratio in order to evaluate the ability of commonly used network models to describe fluid percolation in multiscale porous media and then applied critical path analysis to the prediction of flow permeability. This enabled representation of pores across five orders of magnitude ranging from 0.01 to 1000 μm. These smaller pores are commonly ignored in nonhierarchical (single-scale) lattices commonly used in invasion percolation modelling of capillarity and transport in porous media (Amirtharaj *et al.* 2011) and are beyond the current resolution limits of XRCT used for multiscale 3D pore network analysis (Roels & Carmeliet 2006; Dong & Blunt 2009; Han *et al.* 2009; Hall *et al.* 2013). However, very small pores do not permit fluid flow except under very high pressure gradients, and unlike SEM and MIP, XRCT is nondestructive and can be used for *in situ* imaging of undisturbed sandstone cores. In this study, for example, it was used for pre- and post-injection process imaging of the same core for direct comparison of process–structure–property relationships.

It has been reported that acid dissolution could substantially alter the pore network geometry (and associated heterogeneities), leading to significant time-varying alteration of both the intrinsic permeability and the capillary trapping mechanism (Lamy-Chappuis *et al.* 2014; Armitage *et al.* 2013; Yu *et al.* 2012). This is not usually considered in long-term reactive transport models of candidate saline aquifers and will therefore form the focus of this paper. To help address such shortcomings, the aim of this study was to determine the process–structure–property relationships between the pre- and post-CO_2 injection pore network geometry and the intrinsic permeability. A piece of well-characterised sandstone was subjected to long-term continuous flow of acidic CO_2-rich saline fluid, and we compared the changes observed in this laboratory test to those predicted from modelling. New information gained from this study could provide a useful input into reservoir models to improve accuracy and time-dependent behaviour.

Geological background

The sample rock core for this work is the Lower Triassic Sherwood Sandstone from the Cleethorpes No. 1 borehole, located in the East Yorkshire and Lincolnshire Basin (see Location Map: Fig. 1). The rock unit is known onshore as the Sherwood Sandstone Group and offshore as the Bunter Sandstone Formation (Brook *et al.* 2003). The sample was chosen because of its generic applicability to many potential future UK CO_2 storage schemes, although it is coincidentally the same type of material making up the proposed storage formation for the White Rose CCS project, a contender within the UK CCS Commercialisation Programme.

The Sherwood Sandstone Group is composed generally of a series of marginal and basal breccias which are well-cemented at depth and overlain by a series of sand-dominated fining-upwards cycles representing distal alluvial fan and braided stream deposits (Allen *et al.* 1985). The borehole log (Fig. 2) showed the Sherwood Sandstone Group to be a 398 m thick, uniform deposit presently at depths from 1100 m to 1498 m in this borehole with a mean porosity of 19%, containing formation water at a mean temperature of 50°C and a salinity of 35–80 g l^{-1} (Downing *et al.* 1985). Downing *et al.* (1985) described it as mostly medium-grained, cemented sandstone that is locally micaceous and firm to friable. The intergranular cement is predominantly dolomite but with some anhydrite and negligible calcite. Below 1455 m, the grain size decreases to give an increasingly argillaceous fine to medium-grained sandstone with sporadic thin mudstone and siltstone bands. The Sherwood Sandstone Group is underlain by evaporate and a 308-m-thick Magnesian Limestone sequence (Downing *et al.* 1985).

According to Downing *et al.* (1985), the geophysical logs of the Sherwood Sandstone Group showed very rapid variations with some variation in bulk physical properties over intervals ≥3 m, indicating relatively thin cyclic variations in lithology. The geothermal gradient from 1095 m to 1490 m was 30.13°C km^{-1}, resulting in an estimate temperature variation within the Sherwood Sandstone ranging from 44°C (top) to 55.7°C (bottom) and a mean temperature of 49.8°C. At Cleethorpes, the most porous zones are beneath 1300 m where for 160 m, the average porosity is typically >20% and >24% for about 30 m. Laboratory measurements on sandstones cores produced permeabilities between 106 and 1657 mD using N_2 as the test fluid. The cored sample used for this study was taken from a lower permeability (<<100 mD) horizon between a

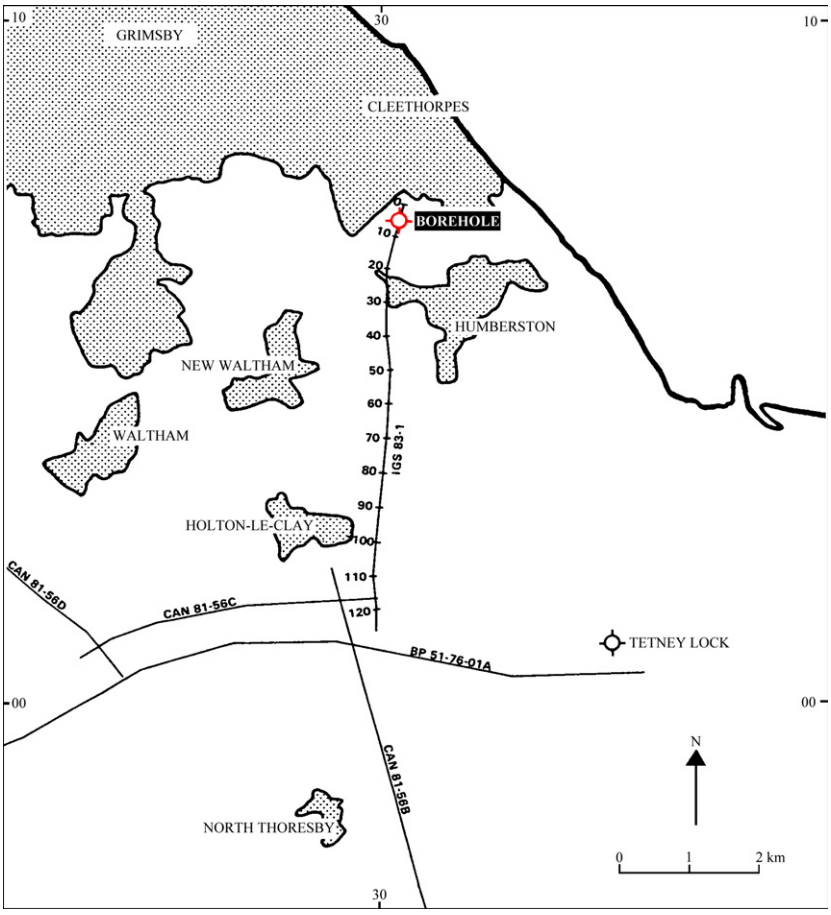

Fig. 1. Cleethorpes borehole #1 location map (adapted from: Downing *et al.* 1985).

depth of 1311.99 m to 1312.27 m, as indicated on the borehole log (Fig. 2) (Downing *et al.*1985).

METHODS AND CHARACTERISATION

The prepared sample was a subcore 150 mm in length and 44 mm diameter. The intention was to force flow across the bedding planes in order to represent porosity alteration near the point of CO_2 injection in a reservoir. Sample selection was partly governed by core availability; in this case, the core was not wide enough to allow a sample of the required size to be taken parallel to bedding. It was treated by placing in a flow cell (see Fig. 3) and surrounded by a Teflon (PTFE) membrane. A higher pressure confining fluid (confining pressure = 20.1 MPa) surrounded the sample such that the Teflon membrane tightly fitted the sample and ensured that the CO_2-rich fluid flowed through the sample (flowing system pressure = 20 MPa). The CO_2-rich fluid that flowed through the sandstone sample was prepared by dissolving CO_2 into 0.5 M NaCl (saline) water inside a Baskerville 3-l continuously stirred, titanium-lined autoclave. The fluid was kept at a constant temperature of 140°C and pressurised with CO_2 to 20 MPa (200 bars). The pressure and salinity were chosen to reflect the *in situ* conditions of a typical saline aquifer, but with elevated temperature (T = 140°C) in order to increase the speed of chemical reactions within the pore network. The 20 MPa fluid pressure equates to a depth of 2000 m, where potential depths for reservoirs in the North Sea vary from 800 m (*e.g.* Sleipner) to around 4500 m (in the N. North Sea, *e.g.* South Brea, Miller). At these depths, temperature varies between 30 and 150°C and so a depth of 2000 m is in the mid-range for potential CO_2 storage sites. As the *in situ* temperature had an average value of *c.* 50°C, the experimental value is approximately 2.8 times greater. For many silicate minerals, a useful rule of thumb is that a doubling of temperature increases reaction rate by an order of magnitude. This arises from the Arrhenius equation on the temperature dependence of reaction rates, *that is* that the reaction rate typically doubles for every 10 degree Celsius increase in temperature (Pauling 1988). This suggests acceleration of the reaction rate by approximately 60 times. Equilibrated CO_2-rich solution was continuously pumped through the reaction flow cell containing the rock core for a period of 3 months. Throughout the duration of the 3-month flow-through experiment, out-flowing fluid samples were collected at run pressures (*i.e.* without degassing) using a piston separator once per week. These fluid samples were used to determine the reduced iron, pH, bicarbonate

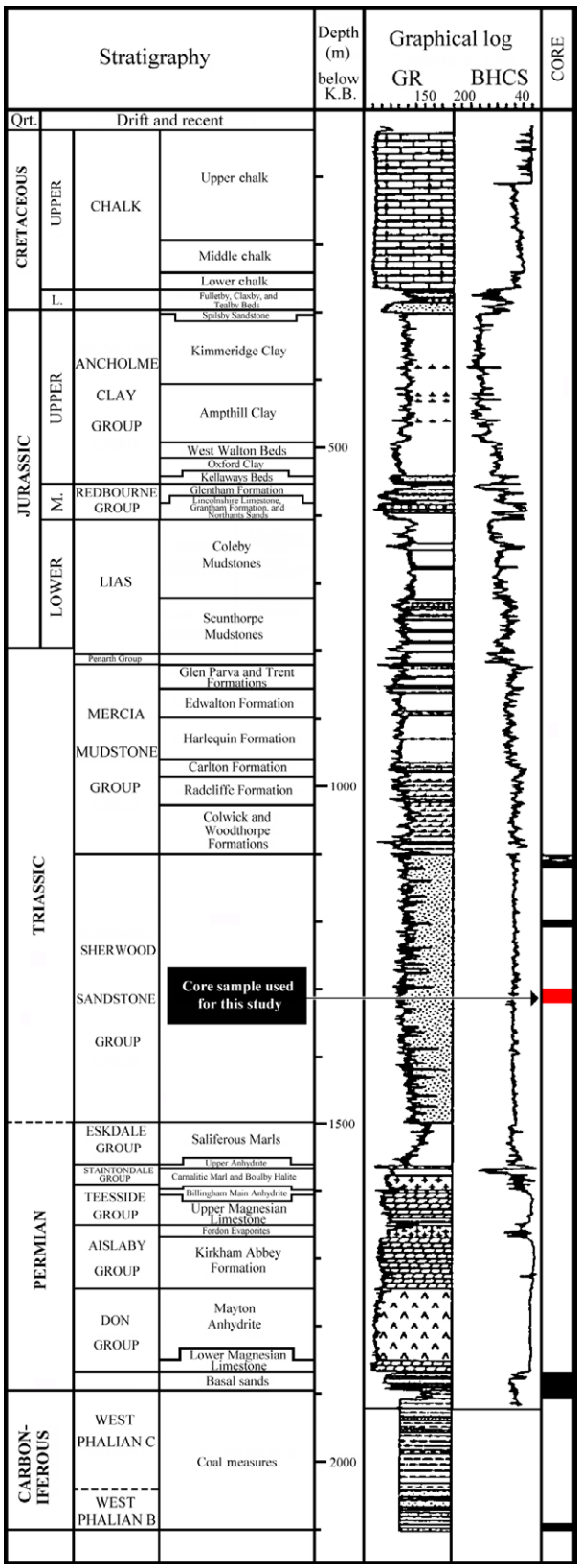

Fig. 2. Cleethorpes borehole #1 log. **Note: Depths are below Kelly Bushing (K. B.) which was 12.16 m above ordnance datum (adapted from: Downing *et al.* 1985).

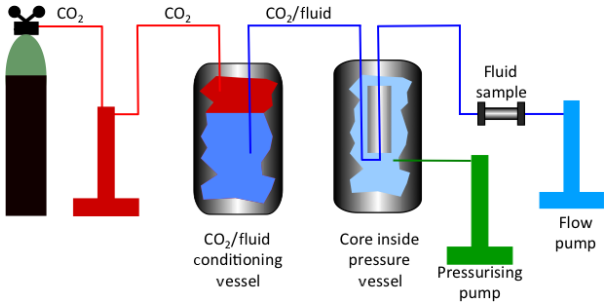

Fig. 3. CO_2 flow-through experimental apparatus and set-up.

measurements, cation and anion analysis. The results from chemical analysis of the out-flowing fluid sample are given in Table 1.

Scanning electron microscopy (SEM)

SEM was conducted using a Philips XL30 with field emission gun (FEG) and Oxford Instruments Inca model energy-dispersive X-ray spectrometer (EDS), which can achieve 133 eV resolution of the Mn K_α peak at full width half maximum (FWHM). Subsamples were prepared by sectioning using a water-cooled abrasive cutter, followed by sonication in industrial methylated spirits (IMS) for ≥2 min followed by hot air blow drying and vacuum cold mounting in epoxy resin. Mounted samples were ground using 240, 400, 800, 1200 wet silicon carbide paper followed by polishing using 6 μm then 1 μm diamond paste, and Pt sputter coated at a rate of 6–7 nm min^{-1} for 90 sec. Micrographs were recorded using a backscattered electron (BSE) detector supplied by K. E. Developments. Micrograph image analysis was conducted using IMAGEJ software v1.44p 32-bit. The images were scaled against the micrograph scale bar and then cropped so as to exclude the scale bar from the image analysis that followed. The contrast and brightness were manually adjusted to bracket the histogram, and a 1px median filter was applied. This resulted in a bimodal histogram and so the intermodes automatic threshold algorithm was used to produce a binary image of the porosity. The standard watershed algorithm was applied in combination with the dark background intermodes automatic threshold to produce binary images of the separated grain structure. Pore and grain size distribution analyses were completed using the 'analyse particles' command across the range 0 μm^2–infinity.

Mercury intrusion porosimetry (MIP)

Pore size distribution and porosity analysis by mercury intrusion porosimetry (MIP) experiments were carried out using a Micromeritics Autopore IV 9500 with ± 0.1 μl

Table 1 Chemical analysis of flow-through fluid.

Sample	t_{int} h	t_{tot} h	pH	HCO_3 mg l^{-1}	HCO_{3corr} mg l^{-1}	Fe(II) mg l^{-1}
1	0.0	0.0	—	—	—	—
2	167.5	167.5	6.53	252.0	1008.0	5.3
3	144.3	311.8	6.24	232.7	930.8	3.2
4	213.8	525.5	6.42	260.1	1040.4	50.6
5	140.5	837.5	6.62	222.0	888.0	15.1
7	169.5	1007.0	6.24	233.8	935.2	12.5
8	145.7	1152.8	6.27	245.0	980.0	14.0
9	195.8	1348.5	6.28	260.0	1040.0	16.6
10	163.5	1512.0	6.23	261.7	1046.8	18.7
11	195.0	1707.0	6.17	268.2	1072.8	19.6
12	334.7	2041.7	6.26	287.1	1148.4	20.5
13	118.3	2160.0	6.21	294.1	1176.5	18.5
14	169.5	2329.5	6.17	294.8	1179.2	—

accuracy. Blank corrections were made before the experiments and subsamples of pre- and post-treated sandstones were first evacuated at 6.7 Pa to remove physisorbed water from the pore walls. Equilibration times of 10, 30 and 50 sec were evaluated to determine the influence on the position of intrusion and extrusion curves. The MIP data were analysed using POREXPERT software package (Environmental and Fluid Modelling Group, University of Plymouth, Plymouth, UK) to simulate the pore network as a series of identical interconnected unit cells (1000 nodes equally spaced in a Cartesian cubic-close-packed array) with periodic boundary conditions, and having the same percolation characteristics as those derived from the experimental data. The experimental data were fitted using an annealed simplex algorithm, which works to find the global minima for a five dimensional surface. To simulate mercury intrusion, a computational representation of fluid was applied to the top face (maximum z) of the unit cell only and percolated in the $-z$ plane. The throat skew, throat spread, pore skew, connectivity and short range size autocorrelation were adjusted by the Boltzmann-annealed amoeboid simplex to give a close fit to the entire mercury intrusion curve.

Measurement of permeability

Prior to testing, the bulk porosity was determined gravimetrically using a digital balance to ±0.01 g accuracy at ambient temperature, 20°C ±2. Saturated mass and displaced volume (mass) were recorded after saturating the samples in deionised water for 24 h, and dry mass was recorded after oven drying to constant mass at 105°C. The intrinsic permeability for saturated pre- and post-treatment sandstone samples (44 mm dia.) was determined in the $-z$ direction using a Trautwein triaxial permeability cell and the standard (saturated flow) Darcy equation. Note that the $-z$ plane is subperpendicular to the sedimentary bedding planes (Fig. 4). Samples were sheathed with a latex triaxial membrane and sealed to the end plattens using elastomer o-rings with sintered brass filter plates. An applied cell (radial confining) pressure of 655 kPa (6.55 bars) was used, with an inlet pressure of 620 kPa (6.20 bars) and a backflow pressure of 586 kPa (5.86 bars). The fluid was de-aired water at a temperature of 20°C ±2 giving a dynamic fluid viscosity of 0.001 Pa s.

X-ray computed tomography (XRCT) with image analysis and CFD

The rock core sample (L = 150 mm, ϕ = 44 mm) was prepared for X-ray computed tomography (XRCT) by wrapping in parafilm and imaged both before and after the 3-month CO_2 flow-through experiment (*i.e.* pre- and post-treatment). The core was scanned using a Phoenix Nanotom 180NF XRCT system (GE Sensing and Inspection Technologies, GmbH, Wunsdorf, Germany) with maximum electron acceleration energy of 120 kV and acquiring 1040 projection images at a spatial (voxel) resolution of 22 μm. Sample orientation during scanning was defined with reference to the direction of the incident X-rays as follows: ZX parallel and normal (-y plane), ZY parallel and horizontally perpendicular (-x plane), XY vertically and horizontally perpendicular (-z plane). Projection images were reconstructed using the back projection algorithm in the 'DATOS|X REC' software. No corrections were required for beam hardening or sample displacement artefacts.

Initial XRCT image analysis was conducted using IMAGEJ software v1.44p 32-bit. The image stack was converted to 8-bit grey scale before scaling to 22 μm resolution and then cropping the image to a representative region (approx. 4 cm^2) to remove any potential edge effects. The contrast and brightness were manually adjusted to bracket the histogram, no filters were applied, and the Yen automatic threshold algorithm was used to segment the pore network and produce a binary image stack. One pass of the noise filter was applied, followed by a remove binary outliers filter set to 1 pixel radius and threshold = 50. Pore size distribution was completed using the 'analyse particles' command across the range 1936 μm^2–infinity (*i.e.* minimum area segmented feature = 2 × 2 px). This enabled 3D projection of the sandstone skeleton and pore network. The minimum cover fractal dimension and lacunarity were both determined as a function of sample depth, d along the z-axis of the core using IMAGEJ software v1.44p 32-bit with FracLac v2.5 by applying the standard box count method at grid size = 5. Pore-scale computational fluid dynamics (CFD) was conducted by first generating a 3D surface file of the segmented pore network using FEI Avizo Fire v8.1 and then used in conjunction with FEI XLab Hydro. The latter was used to solve the volume-averaged form of the Navier–Stokes equations by transforming to the tensorial problem in Eq. 4, and then applying the finite

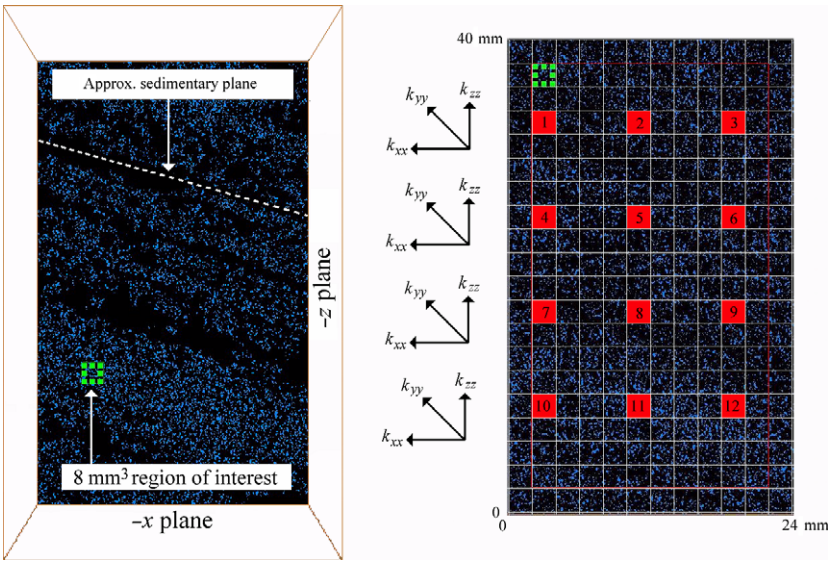

Fig. 4. XRCT orthoslice XZ projections of segmented porosity showing grid positions for (subvolume) regions of interest with respect to sandstone lithology.

volume method with discretisation on a staggered grid (assuming isotropic voxels) (Harlow & Welch 1965; Chorin 1967; Gray 1975).

$$\begin{cases} \nabla^2 \underset{D}{\Rightarrow} & \vec{\nabla}\cdot\vec{\vec{D}} = \vec{0} \\ - & \vec{\nabla}\,\vec{d} = \vec{\vec{I}} \end{cases} \tag{4}$$

A no slip boundary condition was imposed at the rock–fluid interface, and the solution to Eq. 2 was achieved by calculating the mean value of $\vec{\vec{D}}$ over the volume V (see Eq. 5) (Harlow & Welch 1965; Gray 1975).

$$\vec{\vec{k}} = \frac{1}{V}\int_V \vec{\vec{D}}\,\mathrm{d}V \tag{5}$$

An array of twelve 2 × 2 × 2 mm cubic regions (V = 8 mm^3) were identified for analysis on pre- and post-treated samples, see Fig. 4. Calculation of the intrinsic permeability tensor enabled the anisotropy (*i.e.* its dependence on flow direction) to be statistically assessed within the context of the sandstone lithology, and scale-up for direct comparison of the mean k values with those determined by experimental permeability measurements.

RESULTS

The gravimetrically determined bulk porosity of the pre-treatment sample was 18%, which increased to 25% post-treatment. Following petrographic SEM-EDS analysis (Fig. 5 A-C), the pretreated sample was characterised as a close-packed granular structure primarily comprising quartz sand grains (B-2), some of which have significant K-feldspar overgrowth (A-1), with additional K-feldspar grains (B-3), clay, mudstone and carbonate clasts containing detrital K-feldspar or iron oxide fragments (B-4), and partial intergrain cementation by dolomite. Post-treated samples showed significant increase in pore area fraction (see below), primarily through creation of secondary porosity (C-5) due to grain dissolution and with visible roughening of pore walls from grain etching. Dissolution of K-feldspar overgrowth from quartz grains (6) and fully or partially dissolved K-feldspar grains (7) is apparent. Remnants of clay-clothed particles reveal the shadow of dissolved grains (8) and surround post-treatment secondary porosity. 2D image analysis of grain size distribution, using ten representative SEM micrographs with 500 μm scale bar per sample (see example Fig. 5D), shows that the mean cross-sectional area reduces from $5.1{\cdot}10^{-3}$ μm^2 to $4.8{\cdot}10^{-3}$ μm^2 after treatment, whilst mean granular perimeter length reduces from 250.4 μm to 245.2 μm (Fig. 6). As the bulk fabric composition is mainly quartz grains, it was assumed that mass loss occurred primarily due to acid dissolution of the intergranular cements and the K-feldspar grains, as supported by observations of apparent roughening along the pore walls of post-treatment samples (Fig. 7).

Figure 8 shows the increase in cumulative Hg intrusion associated with increased pore volume (caused by dissolution) with a high degree of extrusion capillary entrapment. The data for 30-sec equilibration time are presented, where the mean standard deviation in intruded volume between 10, 30 and 50 sec equilibration times was 0.22% (prereacted) and 1.63% (postreacted). Detailed analysis of this data (Fig. 9) shows that the (pore) cavity/throat volume ratio is 1 at the XRCT resolution limit (*i.e.* corresponding to a mean pore diameter of 44 μm; 2 × 2 px). Pore volume, $V_{p,}$ below this limit, the cavity/throat ratio is < 1 and decreases linearly against the log of the pore diameter, d such that $V_p \approx \log10(d)$. Above the resolution limit, the cavity/throat ratio is >1 and so ink bottle (or saccate) pores occur all of which are detectable by XRCT.

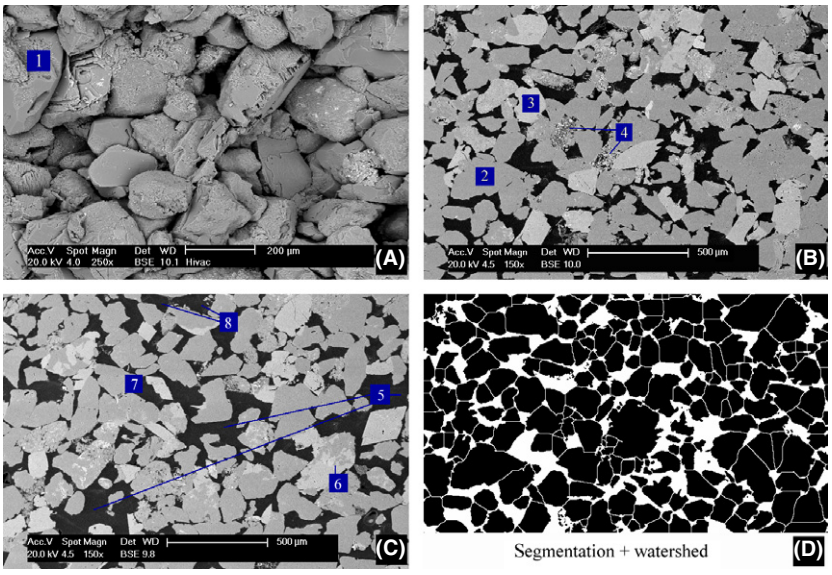

Fig. 5. Annotated BSE micrographs of (A) a post-treatment cleaved surface showing grain morphology, packing and cementation, (B) a pretreatment polished cross section, (C) a post-treatment polished cross section and (D) an example segmented image with watershed grains produced from Fig. 5 (B)

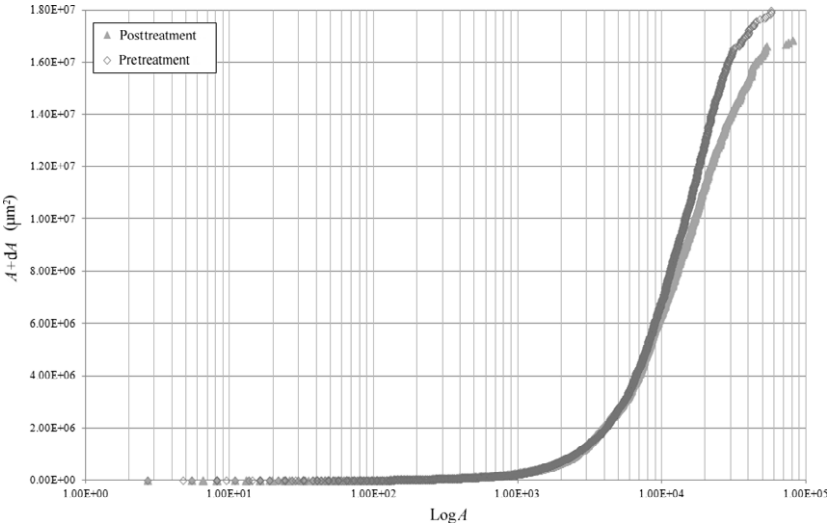

Fig. 6. Mean cross-sectional grain size distribution for pre- and post-treatment determined from segmented and watershed BSE micrographs.

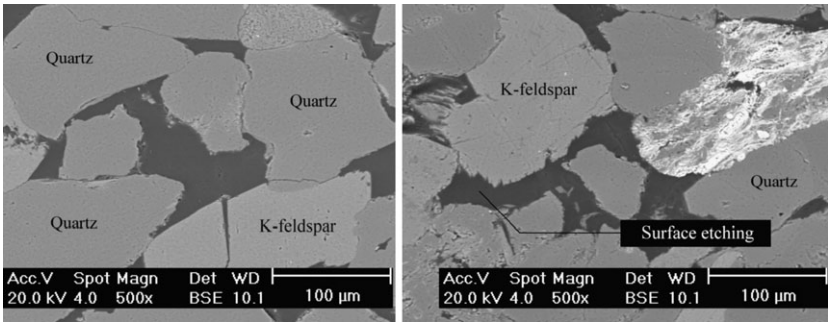

Fig. 7. Annotated BSE micrographs showing (left) pretreatment grain morphology and (right) post-treatment surface roughening and partial grain dissolution.

Observations of the segmented porosity made using XRCT for pretreatment and post-treatment are shown in Fig. 10A,B, respectively. Analysis of the XRCT pore size distribution showed an increase in the number of pores at, or above, a mean cross-sectional area of 40 000 µm^2, which corresponds to a cylindrical pore diameter of 112.8 µm (Fig. 11). The magnitude of the velocity flow field, calculated from the intrinsic permeability solution

to the Navier–Stokes equation (Eq. 5), was mapped as a series of illuminated streamlines onto a cutaway 3D volume render of the pore network. Note that an identical velocity scale colour map was applied in both cases. This enabled visualisation of the critical flow pathways that control the intrinsic permeability, k for both pre- and post-treatment samples (Fig. 12).

The pretreatment, pore wall fractal dimension, D_f, has a mean value of 1.68 and varies as a function of depth from 1.62 to 1.74 (± 0.6). The post-treatment sample shows an increase in the mean fractal dimension, D_f, to 1.84 with a standard deviation of less than ± 0.1 (see Fig. 13). This is a useful statistical metric for the increase in apparent surface roughness, *that is* dissolution of the pore walls by the CO_2-saturated fluid. The lacunarity has also been calculated here as a function of depth, $L(d)$, for use as a scale-dependent measure of spatial heterogeneity that describes the distribution of gaps within a set of fractal patterns at multiple scales. Lacunarity, L, was first introduced by Mandelbrot (1982) to distinguish between different patterns having the same fractal dimension. Latterly, Dong (2000, 2009) proposed a new lacunarity estimation method for greyscale image surfaces based on the gliding-box algorithm introduced by Allain & Cloitre (1991) and a differential box counting method in fractal dimension estimation proposed by Sarkar & Chaudhuri (1992). In this study, $L(d)$ was found to be highly variable throughout the pretreatment sample (where the mean L is 0.45 ± 0.15) compared to the post-treatment sample, in which mean L reduces to 0.25 with $L(d)$ variance ± 0.05 (see Fig. 14).

The experimental results for intrinsic permeability (tested under $-z$ plane flow direction) of the bulk pre- and post-treatment samples are presented in Table 2. The variation of localised intrinsic permeability within the bulk samples, determined by pore-scale modelling inside twelve 8 mm^3 regions of interest (Fig. 4), is shown in Table 3. The data show that the variation in sedimentary packing density, which occurs at cm-scale along the -z plane within the bulk, caused the tensorial intrinsic permeability to vary by more than a factor of ten. The bulk properties for each (pre- and post-treatment) sample were calculated from the mean of all twelve regions of interest to give a global permeability tensor (Eqns. 4 & 6). The intrinsic permeability of the post-treatment sample increased by one order of magnitude compared to the pretreated, and a direct comparison shows very close agreement between the modelled and experimental results. Both tensors show the bulk permeability to be anisotropic having almost equal value in -z and -y planes but with a 68% higher value in the -x plane (parallel to sedimentary bedding planes) for the pretreated sample, reducing to only 30% higher for the post-treated sample.

$$\bar{k}_{pre} = \begin{pmatrix} 0.0074 & 0.0001 & 0.0011 \\ 0.0008 & 0.0044 & 0.0006 \\ 0.0016 & 0.0009 & 0.0044 \end{pmatrix} (\text{unit} : \mu m^2) \quad (4)$$

$$\bar{\lambda}_{pre} = \begin{pmatrix} 0.0091 \\ 0.0036 \\ 0.0032 \end{pmatrix}; \quad \bar{v}_{pre} = \begin{pmatrix} -0.3821 & -0.0227 & -0.1241 \\ 0.0125 & 0.3073 & 0.0180 \\ -0.0832 & 0.0889 & 0.5123 \end{pmatrix} \quad (5)$$

$$\bar{k}_{post} = \begin{pmatrix} 0.1432 & 0.0069 & 0.0169 \\ 0.0101 & 0.1110 & -0.0174 \\ 0.0153 & -0.0171 & 0.1100 \end{pmatrix} (\text{unit} : \mu m^2) \quad (6)$$

$$\bar{\lambda}_{post} = \begin{pmatrix} 0.22336 \\ 0.09356 \\ 0.04729 \end{pmatrix}; \quad \bar{v}_{post} = \begin{pmatrix} -0.08238 & -0.09280 & 0.02050 \\ -0.22420 & 0.09177 & 0.08642 \\ 0.02536 & -0.01230 & 0.61139 \end{pmatrix} \quad (7)$$

DISCUSSION

The gravimetrically determined bulk density for pretreated samples is in general agreement with anticipated values for the Cleethorpes borehole in Sherwood Sandstone at 1300–1350 m depth suggested in previous studies (Downing *et al.* 1985). The SEM-EDS observations are consistent with those of an extensive prior study involving characterisation of the Cleethorpes No. 1 borehole; the reader is referred to an earlier report for additional SEM micrograph images (West *et al.* 2011). The post-treatment increase suggests significant mass loss by dissolution of mineral species into the flowing CO_2-saturated fluid. Mass loss and increased porosity appeared to occur primarily due to dissolution of intergranular cements and K-feldspar grains, with some associated loss of attached clay, carbonate and mudstone clasts. Bulk powder X-ray diffraction (XRD) revealed no evidence of carbonate product formation after processing and that only dissolution must have had occurred. Therefore, this flow-through experiment can be said to either represent early-stage CO_2 injection (near to the point of injection), or later stages if a reaction front occurs at the leading edge of the CO_2 plume.

MIP analysis revealed no significant difference, between pre- and post-treatment samples, in the cavity/throat volume ratio at diameters ≤100 μm. This suggests that no dissolution had occurred in pores of this diameter and so when the cavity/throat volume ratio is ≤1, capillary entrapment is perhaps sufficiently high for the fluid phase to be

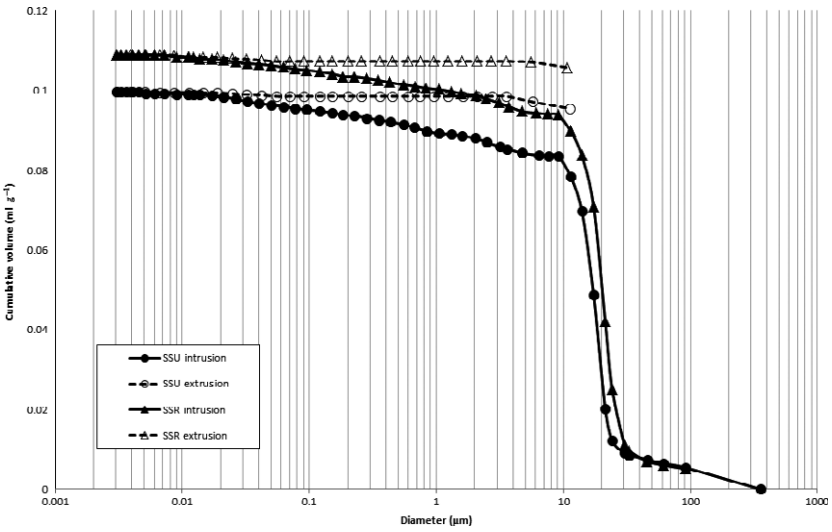

Fig. 8. MIP cumulative intrusion versus pore throat diameter for pre- and post-treatment samples.

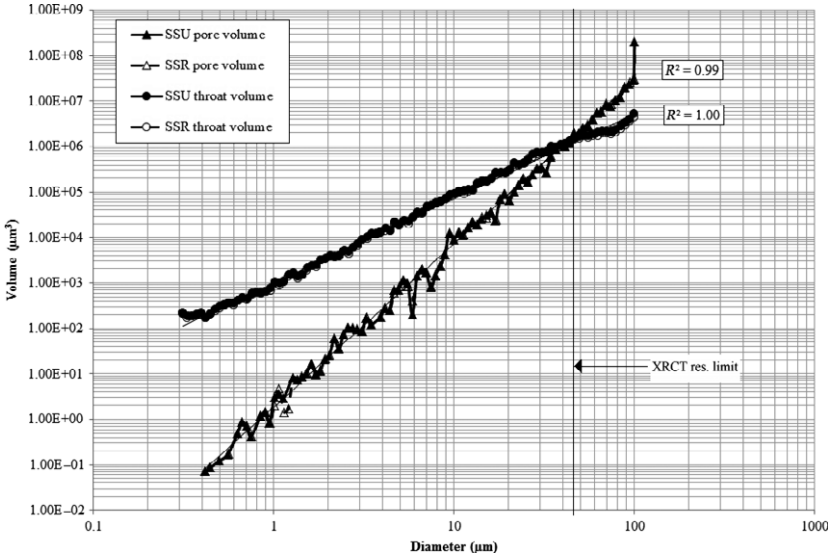

Fig. 9. Log*D*/Log*V* plot for pore throats and pore cavities derived from MIP pore network models for pre- and post-treatment samples.

immobile; *that is,* dissolution occurs in pores that are sufficiently wide to allow measurable fluid flow velocity. At some point >>1, the capillary entrapment becomes sufficiently low that the fluid phase is mobile and able to move under a moderate pressure gradient, thus enabling pore network dissolution to occur. It also indicates that all significant dissolution (resulting in pore network alteration) occurred in pores above *c.* 100 µm diameter, as supported by XRCT analysis (see Fig. 10).

The relative dilation of post-treatment pore area appears to increase in relation to initial (pretreatment) pore area, which suggests that dissolution mass loss has a positive relationship with pore-scale fluid flow velocity; *that is,* the critical flow pathways are preferentially widened. Critical flow paths are defined here as continuous channels of interconnected pores through which fluid can percolate along a given axis (in this case $-z$). Following superposition of the velocity flow field, from the finite volume intrinsic permeability solution to the Navier–Stokes equations, the pretreatment sample was characterised by a small number of low velocity, highly tortuous critical flow paths. The effect of the increased secondary porosity (from interparticle cement and grain dissolution) in the post-treatment sample was to substantially increase the number of critical flow paths and the mean velocity within the pore network, with apparent reduction in tortuosity. This resulted in a significant increase in post-treatment intrinsic permeability (Eq. 6). The fluid flow velocity reaches very high local values at the throats of saccate ('ink bottle') pores (Figs 12 and 15), which suggests that acid dissolution could be accelerated at these points within the pore network.

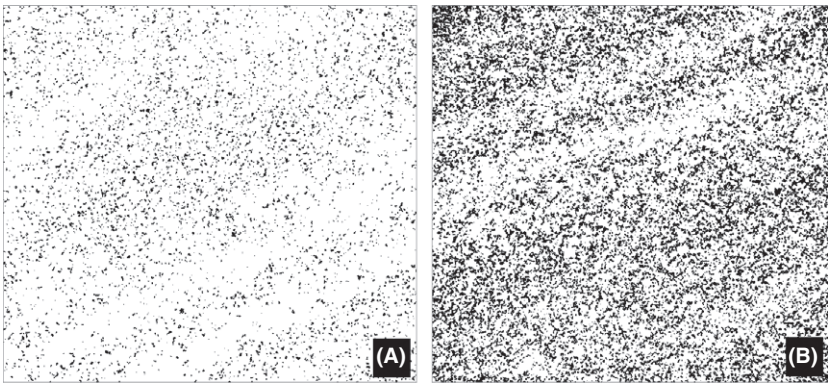

Fig. 10. Representative XRCT orthoslice XY projections of segmented porosity for (A) pretreatment and (B) post-treatment.

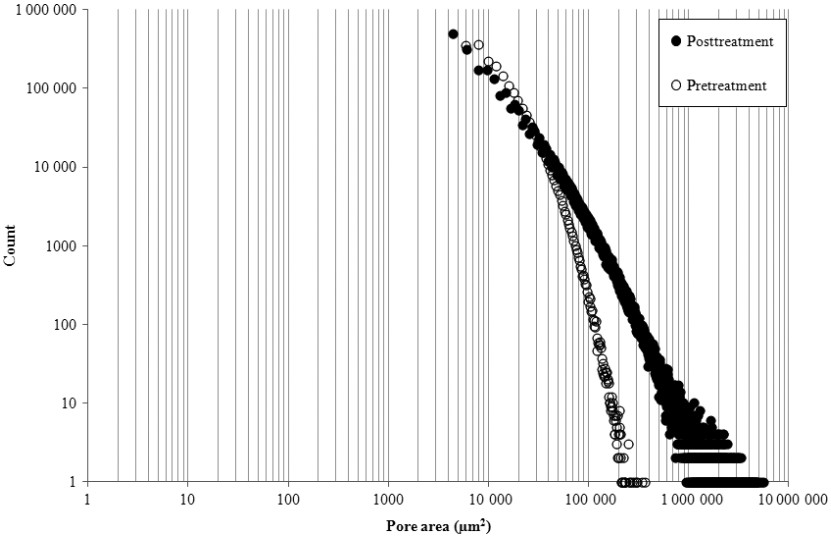

Fig. 11. Mean cross-sectional pore area distribution for pre- and post-treatment XRCT segmented porosity.

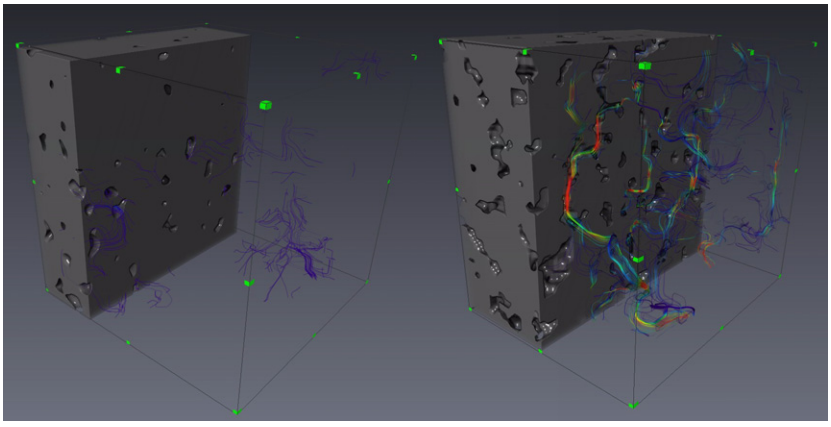

Fig. 12. 3D volume render cutaway of the segmented porosity in (left) pretreatment and (right) post-treatment samples. Illuminated streamlines indicate the $-z$ plane principle flow paths within the pore network, and the colour map corresponds to magnitude within the velocity flow field.

The substantial reduction in $D_f(d)$ for the post-treatment sample indicates that dissolution rate is nonuniform as a function of position along the $-z$ plane and preferentially erodes the (initially) less accessible pores. This is consistent with the previous observations of high fluid flow velocity occurring at the throats of saccate pores in the post-treatment sample (Figs 12 and 15) and supports the hypothesis that this may result in enhanced acid dissolution. The reduction in the variation of lacunarity as a function of $-z$ plane depth supports our earlier observation that CO_2 injection may have reduced pore wall thickness (reduction in K-feldspar sand grain diameter) by

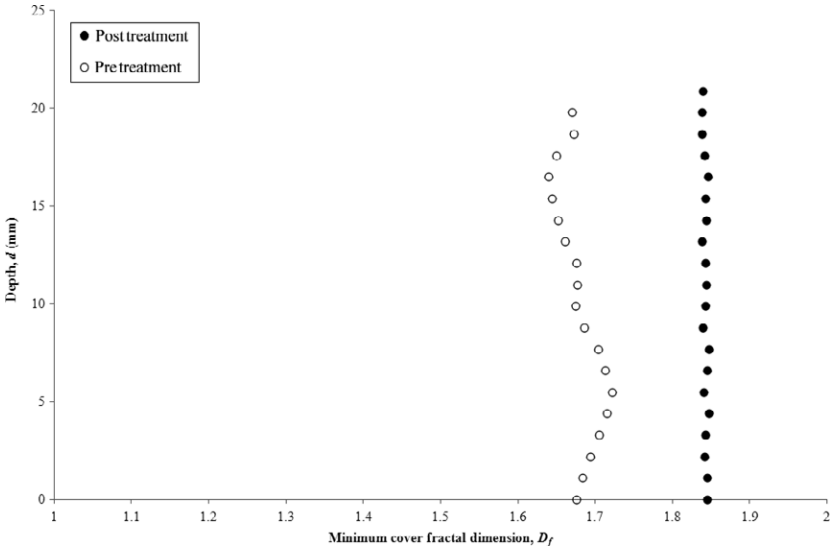

Fig. 13. Fractal dimension as a function of depth, $D_f(d)$, determined from XRCT segmented porosity.

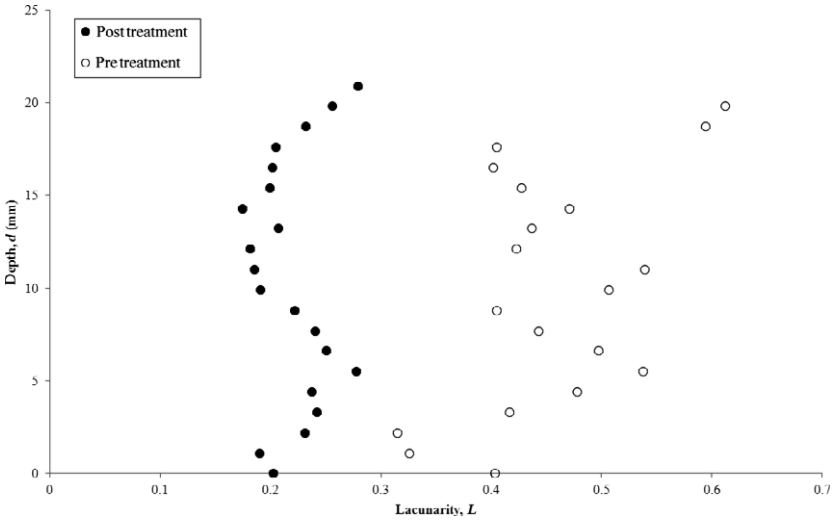

Fig. 14. Lacunarity as a function of depth, $L(d)$, determined from XRCT segmented porosity.

Table 2 Experimental permeability data.

	k_{pre}		k_{post}	
	μm^2	(mD)*	μm^2	(mD)*
Test 1	0.013	(13)	0.113	(115)
Test 2	0.012	(12)	0.114	(116)
Test 3	0.011	(11)	0.132	(134)
Mean	0.012	(12)	0.120	(122)
St. Dev.	0.08%		0.92%	

*1 μm^2 = 1013.2 mD.

Table 3 Mean tensorial permeability as a function of -*z* plane position.

-*z* plane position						
	Pretreatment			Post-treatment		
(Refer Figure 9)	$\bar{k}_{xx}$ μm^2	$\bar{k}_{yy}$ μm^2	$\bar{k}_{zz}$ μm^2	$\bar{k}_{xx}$ μm^2	$\bar{k}_{yy}$ μm^2	$\bar{k}_{zz}$ μm^2
$1–3_{mean}$	0.0015	0.0016	0.0011	0.0120	0.0111	0.0070
$4–6_{mean}$	0.0013	0.0017	0.0016	0.0322	0.0357	0.0315
$7–9_{mean}$	0.0022	0.0039	0.0032	0.0785	0.1058	0.0276
$10–12_{mean}$	0.0246	0.0104	0.0118	0.4500	0.2914	0.3741
$1–12_{mean}$	0.0074	0.0044	0.0044	0.1432	0.1110	0.1100

preferential dissolution of localised regions within the pore network. We tentatively suggest that this corresponds to variations in velocity within the flow net in which localised regions dissolve at a faster rate.

The mean eigenvector tensor clearly shows that the principal flow direction (parallel to pressure drop) is in the –*z* plane for the pretreatment sample (Eq. 5), whilst for post-treatment v_{zz} increases further and both v_{xx} and v_{yy} decrease (Eq. 7). This suggests that the dissolution caused by continuous CO_2-saturated fluid flow in the –*z* plane is

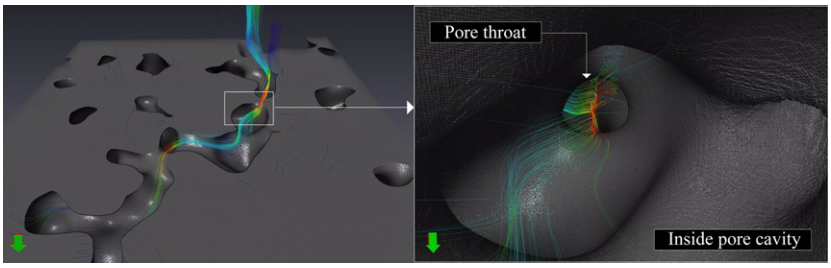

Fig. 15. 3D volume render cutaway of the segmented porosity in the post-treatment sample showing (left) local concentration of high flow velocity at the throats of saccate (ink bottle) pores, and (right) the view of from inside the cavity of a saccate pore looking towards the throat. Illuminated streamline colour map corresponds to magnitude within the velocity flow field.

preferential such that it realigns and enhances the critical flow paths under a global pressure gradient. The mean eigenvalues for the pretreatment sample suggest that the principal permeability is a factor of three greater along the $-x$ plane, which could be anticipated as this is the closest to being parallel with the sedimentary bedding planes (see Fig. 4). It should be noted that the rate of flow in these experiments meant that only active dissolution occurred in the experiment. Had the rate of flow been slower, or the sample much longer, then the fluid composition would most likely have neared or exceeded saturation with secondary phases. In this case, dissolution may have been overtaken by precipitation. Therefore, this work is more appropriate to the region of the rock closer to an injection borehole.

Whilst the sample treatment temperature of 140°C was elevated (from the original sample's conditions), it is not extreme. Potential depths and temperatures for reservoirs in the North Sea vary from 800 m and 30°C (*e.g.* Sleipner) to around 4500 m and 150°C (e.g. in the N. North Sea, *e.g.* South Brea, Miller). The reaction rates at lower temperatures will therefore be slower. As the introduction of CO_2-rich fluids will disturb chemical equilibrium, the observed reactions are still likely to occur though perhaps over much longer timescales. The experimental flow-through tests ran for 3 months and so, due to current equipment access limitations, it was not feasible to periodically scan the samples using XRCT during this stage. We hypothesise that scanning the cores *in situ* at 20.1 MPa confinement pressure would enable quantification of the consolidation effect on pore network geometry and the associated permeability tensor. This is currently unknown and is recommended as a subject for further study.

CONCLUSIONS

(1) Flow of CO_2-saturated saline fluid caused the bulk porosity of a sample of Lower Triassic Sherwood Sandstone, onshore UK, to increase from 18 to 25%.

(2) Mass loss and increased porosity from dissolution of intergranular cements and K-feldspar grains, causing a reduction in mean grain diameter and an increase in apparent pore wall roughness, where the fractal dimension, D_f, increased from 1.68 to 1.84.

(3) Dissolution mass loss appeared to occur primarily in pores above *c.* 100 μm mean diameter and was negligible in pores where the pore throat: cavity volume ratio is ≤1, and capillary entrapment was sufficiently high for the fluid phase to be immobile

(4) Relative dilation of post-treatment pore area appeared to increase in relation to initial pore area, suggesting that rate of dissolution mass loss has a positive relationship with the pore-scale fluid flow velocity.

(5) A significant post-treatment reduction in $D_f(d)$ indicated that the dissolution rate was nonuniform as a function of position along the $-z$ plane, *that is* perpendicular to sedimentary bedding planes. In further support of this observation, the post-treatment eigenvector, v_{zz}, increases still further, whilst both v_{xx} and v_{yy} decrease, indicating that CO_2 saturated fluid transport has enhanced the critical flow path(s) when flowing under a global pressure gradient.

(6) Variation in packing density within sedimentary planes (occurring at cm-scale along the -z plane) caused the intrinsic permeability tensor to vary by more than a factor of ten.

(7) The bulk permeability tensor is anisotropic having almost equal value in -z and -y planes but with a 68% higher value in the -x plane (parallel to sedimentary bedding planes) for the pretreated sample, reducing to only 30% higher for the post-treated sample.

(8) The intrinsic permeability of the post-treatment sample increased by 1 order of magnitude compared and shows very close agreement between the modelled and experimental results. This study also identified the relative effects on permeability tensors close to the injection site, where there is dissolution only, and no precipitation over time.

(9) Research has demonstrated that the full permeability tensor is needed to correctly solve fluid flow problems in a variety of realistic settings (Gupta *et al.* 2001; Settari *et al.* 2001). The permeability tensor data from this work can be used to assign as inputs for the cells in a reservoir model to better describe the effect of sedimentary planes on permeability. This will give more accurate estimates on injectivity and, where there are local faults, enhanced confidence in storage estimates because migration of the injection plume along

-x, *-y* and *-z* planes is more accurately modelled. These data can be used to enable CCS developers to better understand their risk and to mitigate against any potential CO_2 migration or CO_2 injectivity problems.

ACKNOWLEDGEMENTS

The authors wish to acknowledge the support of the Geo-Energy Research Centre (GERC) for funding this research and also Prof P Matthews (University of Plymouth) for support with the use of POREXPERT software package.

REFERENCES

Allain C, Cloitre M (1991) Characterizing the lacunarity of random and determined fractal set. *Physical Review A*, **44**, 3552–8.

Allen DJ, Gale IN, Price M (1985) *Evaluation of the Permo-Triassic Sandstones of the UK as Geothermal Aquifers in Hydrogeology in the Service of Man*, Mémoires of the 18th Congress of the International Association of Hydrogeologists, Cambridge, UK

Amirtharaj ES, Ioannidis MA, Parker B, Tsakiroglou CD (2011) Statistical synthesis of imaging and porosimetry data for the characterization of microstructure and transport properties of sandstones. *Transport in Porous Media*, **86**, 135–54.

Armitage PJ, Faulkner DR, Worden RH, Aplin AC, Butcher AR, Iliffe J (2011) Experimental measurement of, and controls on, permeability and permeability anisotropy of caprocks from the CO_2 storage project at the Krechba Field, Algeria. *Journal of Geophysical Research: Solid Earth*, **116**.

Armitage PJ, Faulkner DR, Worden RH (2013) Caprock corrosion. *Nature Geoscience*, **6**, 79–80.

Bachu S, Bonijoly D, Bradshaw J, Burruss R, Holloway S, Christensen NP, Mathiassen OM (2007) CO_2 storage capacity estimation: methodology and gaps. *International Journal of Greenhouse Gas Control*, **1**, 430–43.

Brook M, Shaw K, Vincent C, Holloway S (2003) *Gestco case study 2a-1: Storage Potential of the Bunter Sandstone in the UK sector of the southern North Sea and the adjacent onshore area of Eastern England*, Sustainable Energy and Geophysical Surveys Programme Commissioned Report CR/03/154N, British Geological Survey.

Chorin AJ (1967) A numerical method for solving incompressible viscous flow problems. *Journal of Computational Physics*, **2**, 12–26.

Chun HC, Giménez D, Yoon SW (2008) Morphology, lacunarity and entropy of intra-aggregate pores: aggregate size and soil management effects. *Geoderma*, **146**, 83–93.

Czernichowski-Lauriol I, Sanjuan B, Rochelle C, Bateman K, Pearce J, Blackwell P (1996) Analysis of the geochemical aspects of the underground disposal of CO_2. In: *Deep Injection Disposal of Hazardous and Industrial Waste: Scientific and Engineering Aspects* (eds Apps JA, Tsang CF), pp. 565–583. Academic Press, Waltham, MA.

Dong P (2000) Test of a new lacunarity estimation method for image texture analysis. *International Journal of Remote Sensing*, **21**, 3369–73.

Dong P (2009) Lacunarity analysis of raster datasets and 1D, 2D, and 3D point patterns. *Computers and Geosciences*, **35**, 2100–10.

Dong H, Blunt MJ (2009) Pore-network extraction from micro-computerized-tomography images. *Physical Review E*, **80**, 036307.

Downing RA, Allen DJ, Bird MJ, Gale IN, Kay RL, Smith F (1985) *Investigation of the geothermal potential of the UK: Cleethorpes No 1 geothermal well – a preliminary assessment of the resource*, British Geological Survey, Keyworth, UK.

Gaus I, Audigane P, Andre L, Lions J, Jacquemet N, Durst P, Czernichowski-Lauriol I, Azaroual M (2008) Geochemical and solute transport modelling for CO_2 storage, what to expect from it? *International Journal of Greenhouse Gas Control*, **2**, 605–25.

Gray WG (1975) A derivation of the equations for multiphase transport. *Chemical Engineering Science*, **30**, 229–33.

Gunter WD, Perkins EH, McCann TJ (1993) Aquifer disposal of CO_2-rich gases: reaction design for added capacity. *Energy Conversion Management*, **34**, 941–8.

Gupta A, Penuela G, Avila R (2001) An integrated approach to the determination of permeability tensors for naturally fractured reservoirs. *Journal of Canadian Petroleum Technology*, **40**, 43.

Hall MR, Mooney SJ, Sturrock C, Matelloni P, Rigby SP (2013) Characterisation of multi-scale pore geometry and correlation with moisture storage function and sorptivity in cement-stabilised soils. *Acta Geotechnica*, **8**, 67–79.

Han M, Youssef S, Rosenberg E, Fleury M, Levitz P (2009) Deviation from Archie's law in partially saturated porous media: wetting film versus disconnectedness of the conducting phase. *Physical Review E*, **79**, 031127.

Harlow FH, Welch JE (1965) Numerical calculation of time-dependent viscous incompressible flow of fluid with free surface. *Physics of Fluids*, **5**, 317.

Holloway S (1996) *The Underground Disposal of Carbon Dioxide. Final Report for the Joule II Programme*, British Geological Survey, Keyworth, UK.

Katz AJ, Thompson AH (1985) Fractal sandstone pores: implications for conductivity and pore formation. *Physical Review Letters*, **54**, 1325–8.

Lamy-Chappuis B, Angus D, Fisher Q, Grattoni C, Yardley BWD (2014) Rapid porosity and permeability changes of calcareous sandstone due to CO_2-enriched brine injection. *Geophysical Research Letters*, **41**, 399–406.

Leith SD, Reddy MM, Ramirez WF, Heymans MJ (1996) Limestone characterization to model damage from acidic precipitation: effect of pore structure on mass transfer. *Environmental Science and Technology*, **30**, 2202–10.

Mandelbrot BB (1982) *The Fractal Geometry of Nature*. Freeman, San Francisco.

Matter J, Keleman P (2009) Permanent storage of carbon dioxide in geological reservoirs by mineral carbonation. *Nature Geoscience*, **2**, 837–41.

Metz B, Davidson O, de Coninck H, Loos M, Meyer L (eds.) (2005) *Intergovernmental Panel on Climate Change (IPCC) Working Group 3 Special Report: Carbon Dioxide Capture and Storage*. Cambridge University Press, Cambridge, UK.

Padhy GS, Lemaire C, Amirtharaj ES, Ioannidis MA (2007) Pore size distribution in multiscale porous media as revealed by DDIF-NMR, mercury porosimetry and statistical image analysis. *Colloids and Surfaces A*, **300**, 222–34.

Pauling LC (1988) *General Chemistry*. Dover Publications, UK.

Quispe JR, Rozas RE, Toledo PG (2005) Permeability–porosity relationship from a geometrical model of shrinking and lattice Boltzmann and Monte Carlo simulations of flow in two-dimensional pore networks. *Chemical Engineering Journal*, **111**, 225–36.

Radlinski AP, Ioannidis MA, Hinde AL, Hainbuchner M, Baron M, Rauch H, Kline SR (2004) Angstrom to millimeter characterization of sedimentary rock microstructure. *Journal of Colloid and Interface Science*, **274**, 607–12.

Rochelle CA, Czernichowski-Lauriol I, Milodowski AE (2004) The impact of chemical reactions on CO_2 storage in geological formations: a brief review, in Baines SJ & Worden RH Geological storage of carbon dioxide 233 UK Geological Society Special Publications, London.

Roels S, Carmeliet J (2006) Analysis of moisture flow in porous materials using microfocus X-ray radiography. *International Journal of Heat and Mass Transfer*, **49**, 4762–72.

Sarkar N, Chaudhuri BB (1992) An efficient approach to estimate fractal dimension of textural images. *Pattern Recognition*, **25**, 1035–41.

Settari A, Walters DA, Behie GA (2001) Use of coupled reservoir and geomechanical modeling for integrated reservoir analysis and management. *Journal of Canadian Petroleum Technology*, **40**, 55.

Vidal D, Ridgway C, Pianet G, Schoelkopf J, Roy R, Bertrand F (2009) Effect of particle size distribution and packing compression on fluid permeability as predicted by lattice-Boltzmann simulations. *Computers and Chemical Engineering*, **33**, 256–66.

West JM, Bateman K, Coombs P, Harrison HM, Holyoake S, AE M, Rushton J, Turner G, Wagner D, Wragg J (2011) *Microbiological effects on transport processes (BioTran) – Data production from column experiments containing Sherwood Sandstone*, BGS Open Report OR/11/058, Keyworth, UK.

Xiao Y, Xu T, Pruess K (2009) The effects of gas-fluid-rock interactions on CO_2 injection and storage: insights from reactive transport modelling. *Energy Procedia*, **1**, 1783–90.

Yu B, Cheng P (2002) A fractal permeability model for bi-dispersed porous media. *International Journal of Heat and Mass Transfer*, **45**, 2983–93.

Yu B, Zou M, Feng Y (2005) Permeability of fractal porous media by Monte Carlo simulations. *International Journal of Heat and Mass Transfer*, **48**, 2787–94.

Yu Z, Liu L, Yang S, Li S, Yang Y (2012) An experimental study of CO_2-brine-rock interaction at *in situ* pressure-temperature reservoir conditions. *Chemical Geology*, **326–327**, 88–101.